Oxidation of austenitic stainless steels in PWR primary water

Antoine Herbelin, Thierry Couvant, Laurent Legras, David Delafosse, Gabriel Ilbevare

Oxidation of austenitic stainless steels in PWR primary water

Antoine HERBELIN[1], Thierry COUVANT[2], Laurent LEGRAS[3], David DELAFOSSE[4], Gabriel ILEVBARE[5]

[1]*Ecole des Mines de Saint Etienne, France, antoine-externe.herbelin@edf.fr*
[2] EDF R&D, *France, thierry.couvant@edf.fr*
[3]EDF R&D, *France, laurent.legras@edf.fr*
[4]*Ecole des Mines de Saint Etienne, France, david.delafosse@emse.fr*
[5]*EPRI, California, gilevbare@epri.com*

Abstract:

304L and 316L SS samples are SCC-tested in PWR water for various conditions: strain level, duration, pH, surface finish. The passive Chromium-rich oxide layer, the consistent oxidation feature, is characterized using Transmission Electron Microscope analysis. EDX analysis and Energy-filtered images are used to map the oxide penetration at the surface of the sample and at contiguous grain boundaries. Statistical data obtained by these characterizations are exploited to considerate the effects of deformation, pH and duration on oxidation. Complementary analyses of intergranular crack initiations allow to invetigate the oxidation phenomenon at grain boundaries and its influence on intergranular cracking.

Keywords: Oxidation, austenitic stainless steels, SCC, PWR, TEM

1. Background

Oxidation is a key phenomenon in the stress corrosion cracking (SCC) mechanisms of stainless steel (SS) in primary water of pressurized water (PWR) reactors: the passive chromium-rich oxide formed at the surface of SS forms a protective barrier from the environment, but also constitutes a boundary where the crack initiation could occur. Previous studies [1] have demonstrated the deleterious effect of plastic deformation on susceptibility of 304L to IGSCC in PWR primary water at 360°C. TEM observation [2] allowed to identify specific interactions between plasticity and oxidation. Oxidation phenomenon needs to be quantified in order to develop predictive models involving interactions between mechanical and environmental effects.

2. Materials

Austenitic alloys tested in this work (304L and 316L) were sampled from 30-mm-thick plates. Chemical compositions and mechanical properties of the materials as manufactured are given in Table 1 and Table 2, respectively. Unlike 316L, 304L contains less than 5% of residual δ-ferrite and is subject to strain-induced martensite transformation: Ms = –133°C, Md_{30} = –3°C, as predicted by Angel [3]. In the 316L heat XY183, Ms = –133°C, Md_{30} = –40°C. The estimated staking fault energy (SFE) of 304L is 24 mJ.m^{-2} and that of the 316L is 33 mJ.m^{-2} [4]. Non-sensitized 304L and 316L were solution-annealed at 1050°C and water quenched. The resulting microstructures, showing no evidence of carbide precipitation, neither in the matrix, nor along the grain boundaries, were characterized using EBSD. The average grain diameter was 27 µm for 304L and 90 µm for 316L. The distributions of misorientation angles were comparable for 304L and 316L, in the range $6° < \phi < 59°$, including twin boundaries ($\phi > 54°$). In both materials, 30 to 50% of boundaries were twin boundaries.

Table 1 – Chemical composition (wt. %).

Material	Heat	C (%)	S (%)	P (%)	Si (%)	Mn (%)	Fe (%)	Ni (%)	Cr (%)	Mo (%)	N (%)	Al (%)
316L	XY183	0.026	0.004	0.033	0.42	1.81	65.75	12.00	17.34	2.57	0.050	-
AISI Requirement for 316L		< 0.03	< 0.03	< 0.045	< 1	< 2		10-13	16.5-18.5	2-2.5	< 0.11	
304L	T2575	0.026	0.002	0.027	0.52	1.49	68.68	9.45	19.23	0.24	0.064	0.033
AISI Requirement for 304L		< 0.03	< 0.03	< 0.045	< 1	< 2		8-10	18-20		< 0.11	

Table 2 – Mechanical properties in air at room temperature.

Material	Heat	$Ys_{0,2}$ (MPa)	UTS (MPa)	El. (%)	HV_{30}
316L	XY183	255	553	63	
304L	T2575	247	582	60	160
RCCM-M220 requirement		> 170	> 500	> 45	126-179

3. Experiments

3.1. Specimens

Most of the TEM characterizations were performed on specific cross-shaped specimens (Figure 1). This specimen geometry and testing procedure allows the testing of SCC in PWR primary water while inducing strain localization and complex loading paths. The details of these specimen and the associated tests have been described in [5, 6].

Cross tests were used to promote strain localization. This design was optimized to obtain strain localization in the cross-area of the specimen during pre-straining and subsequent deformation in primary water. The specimen is not symmetrical through its thickness: only the front face is perfectly plane, designed to allow for easy mechanical polishing, material characterization and local strain evaluation. All characterizations and observations were done on 1 mm^2 area at the center of the specimen's front face.

The sample's surface of interest was mechanically polished down to 0.25 µm abrasive finish in order to remove the superficial cold work due to machining. Electrolytic polishing was then performed to eliminate residual cold work after mechanical polishing. The solution used was a Struers A2 electrolyte containing 73% ethanol, 10% butoxyethanol, 9% water, and 8% perchloric acid. This treatment leaves a chemically-affected layer enriched in chromium in the first few nm from the surface. A plasma cleaning step was thus used to remove this layer possibly affecting subsequent oxidation reactions. The layer was removed using 4.5 kV argon ions at low incidence for 2 minutes to minimize the irradiation damage to the surface.

EBSD characterizations were carried out on the 1 mm^2 area at the center of each specimen. Gold grids (1 mm^2, mesh size = 5 µm) were deposited by electron micro-lithography at the center of the specimens, allowing the quantification of local deformation using image correlations on grid images acquired in a SEM.

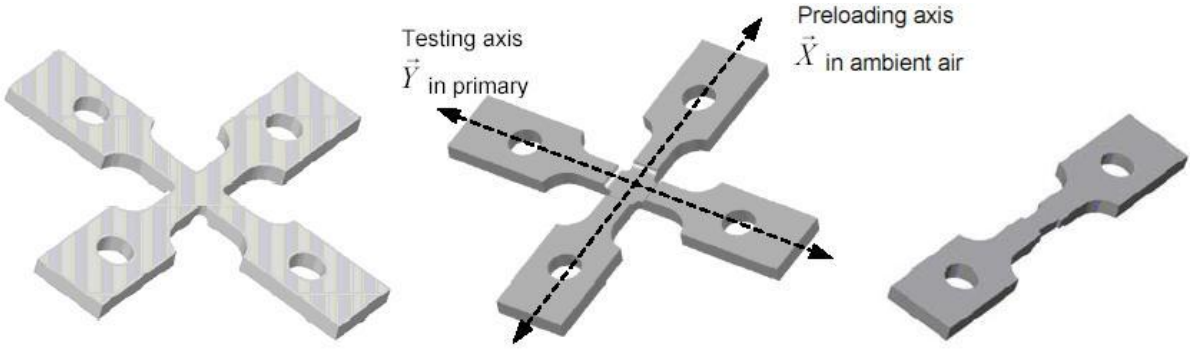

Figure 1 – Cross-shaped specimen

3.2. Pre-deformation and SCC tests on cross-shaped specimens

Pre-deformation of the cross-shaped specimens was achieved through a monotonous tensile deformation along the X axis. After the acquisition of deformed microgrid images in a SEM to characterize the prior deformation, the specimens arms used for pre-straining were cut off and the reduction in section thickness ensured that deformation was localized at the center of the specimen during the second loading stage in simulated PWR primary environment at 360°C.

Specimens were rinsed ultrasonically in ethanol and in distilled water before testing was continued. Tests were carried out in Hastelloy (C-276) autoclaves. The specimens were insulated from the autoclave by oxidized Zircalloy to avoid galvanic coupling. Experiments were conducted under open circuit conditions. The environment was primary water (1000 ppm B as boric acid, 2 ppm Li as lithium hydroxide) at 360°C. The solution was previously de-aerated by evaporating 20% of the initial volume at 125°C, then hydrogen overpressure was introduced (30 $cm^3.kg^{-1}$) and controlled using a Pd-Ag probe. The chemistry was analyzed and validated before each test (B, Li, Cl^-, SO_4^{2-}, F^-). Finally, images of the surface of interest were acquired in a SEM in order to quantify the second deformation and identify SCC initiation sites.

Table 3 – Summary of pre-deformation and test in PWR water for cross-shaped specimen

Material	Specimen	Pre-deformation E_{xx}	Second deformation E_{yy} in PWR water	Duration of the test in PWR water (h)
304L	T112-06	0.09	0.03	519
316L	T217-01	0.07	0.02	720

3.3. Tests on U-bends and tensile specimens at different pH, temperatures and time durations

Other specimens were used: U-bends and 'classical' tensile specimens cut in a 316L tube with an as-received grinded surface. Hardness measurements allowed to estimate the strain level on grinded surfaces to $\varepsilon = 0.025$. For U-bends tests, TEM samples were cut in non-strained parts. Testing conditions are summarized in Table 4.

Table 4 – Summary of non-cross specimens and testing conditions

Material	Heat	Name	Surface finish	Estimated strain level	$pH_{325°C}$	Temperature (°C)	Exposure time (h)
304L	T2575	1171-13	Grinding	0.4	7.2	320	4
304L	T2575	T112-35	Grinding	0.025	7.2	360	17000
316L	XY183	1171H4	Grinding	0.025	8	360	600
316L	XY183	1512-10	Grinding	0.025	9,1	360	240
304L	T2575	1512-22	Grinding	0.025	9,1	360	5000

A short exposure test was carried out in a specifically designed capsule placed in an autoclave (Figure 2). A specimen was introduced in the capsule, after tensile pre-deformation at room temperature (specimen 1171-13, 304L, heat T2575, strained to 40%). The test in primary water at 320°C lasted 6h (2h heating and 4h at 320°C), then a rapid decrease of temperature was obtained by the injection of cold pure water in the capsule (Figure 3). After testing, thin foils were cut to quantify the surface oxides.

Figure 2 – Capsule for short exposure to primary water.

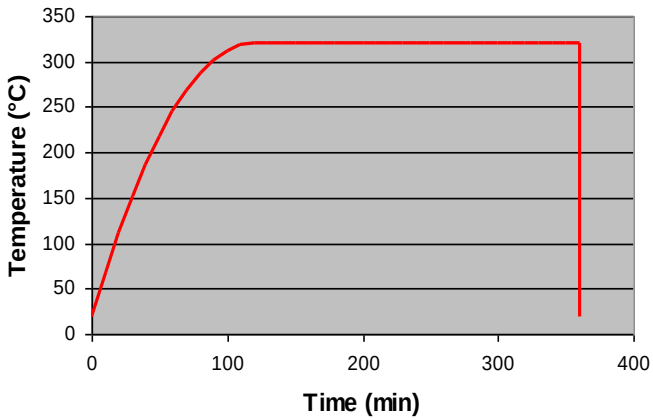

Figure 3 – Evolution of the temperature during testing in capsule.

Three of the specimens were tested [2] at higher levels of alkalinity in order to simulate a possible occluded chemistry. At variance with nominal conditions (1000 ppm B as boric acid, 2 ppm Li as lithium hydroxide), 10 ppm Li was used in a first test, and 400 ppm Li in two other tests. Multeq^{TM} simulations estimated that $pH_{320°C}$ = 7.2 under nominal conditions (2 ppm Li), $pH_{320°C}$ = 8 for the first alkaline test and $pH_{320°C}$ = 9.1 for the other two.

3.4 TEM Analysis

A FEI dual-beam Helios Nanolab was used for preparing cross section thin foils on specifically deformed locations and SCC initiation sites on cross specimens. This dual beam has a Schottky field emission gun column, Ga Focused Ions Beam column, Pt and C gas injection system, carbon selective etching system, EDX detector, Autoprobe internal micromanipulator and 3D EBSD system.

Cross-sections from other specimens were prepared by cutting sections using a slow-speed diamond saw and gluing surfaces of interest with thermosetting epoxy under vacuum. The samples were adjusted and assembled in an insert, and thin foils were cut and polished. Electron transparency was achieved using a dimple grinder down to 20 µm and ion micromilling to perforation.

TEM observations of specimens were performed using a FEI TECNAI G2 FEG STEM equipped with Gatan Imaging Filter, EDAX energy dispersive spectrometer and HAADF detector. Besides conventional TEM and STEM imaging, oxides were characterized using EDS for concentration profiles across layers and EFTEM for elemental mapping.

4. Results

4.1. Oxide formed at $pH_{320°C}$ 7.2 and 360°C on cold-worked material

Several sampling locations were chosen at the surface of the two cross-shaped specimens 1594-T112-06 and 1594-T217-01, based on the deformation measurements and SEM observations of crack initiation. **Figure** 4 and **Figure** 5 give an example of such a correlation for the site 1 on 1594-T217-01. The site was centered on an intergranular crack between two grains exhibiting different levels of deformation. The level of pre-deformation E_{xx} in ambient air and second deformation E_{yy} in primary water corresponding to the sampling for TEM examinations are reported in Table 5.

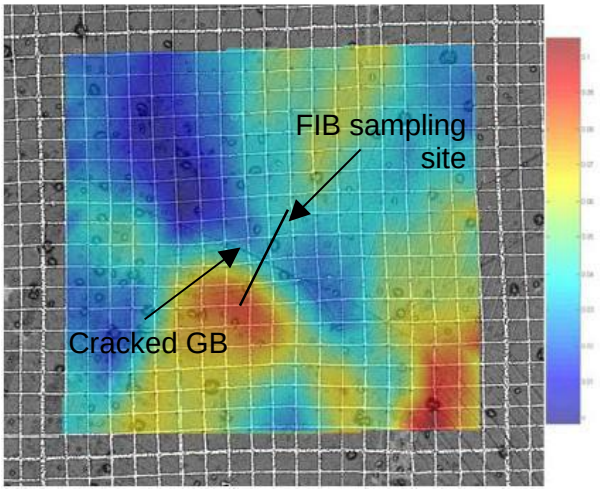

Figure 4 – Pre-deformation *Exx* (in ambient air) on initiation site 1 at the surface of specimen 1594-T217-01 (316L)

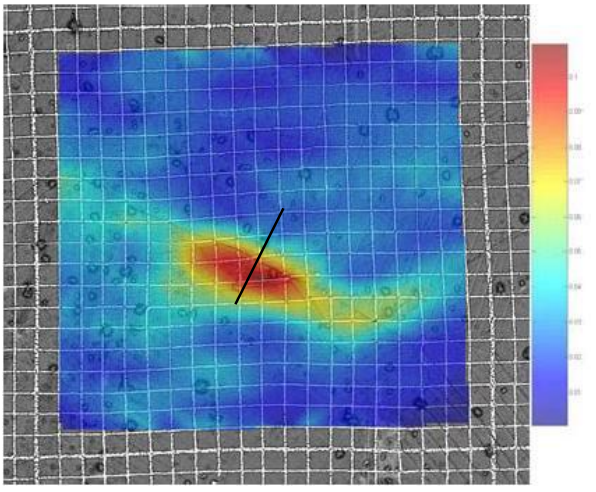

Figure 5 – Deformation Eyy (in primary water) on initiation site 1 at the surface of specimen 1594-T217-01 (316L)

Figure 6 shows a typical oxide formed on strain hardened stainless steels exposed to primary water at 360°C (T112-06, 304L, 7.2 $pH_{320°C}$). The oxide-metal interface was clearly positioned below the grid-oxide interface, indicating the anionic growth of the inner Cr-rich oxide layer in the metal. A preferential oxidation can be also noticed within pre-established shear bands and microtwins from pre-deformation in air. Spinels grew on the inner Cr-rich oxide layer and on the grid. Magnetite was identified. Despite the presence of the inner Cr-rich oxide layer, spinels displayed an epitaxial relationship with the metal substrate.

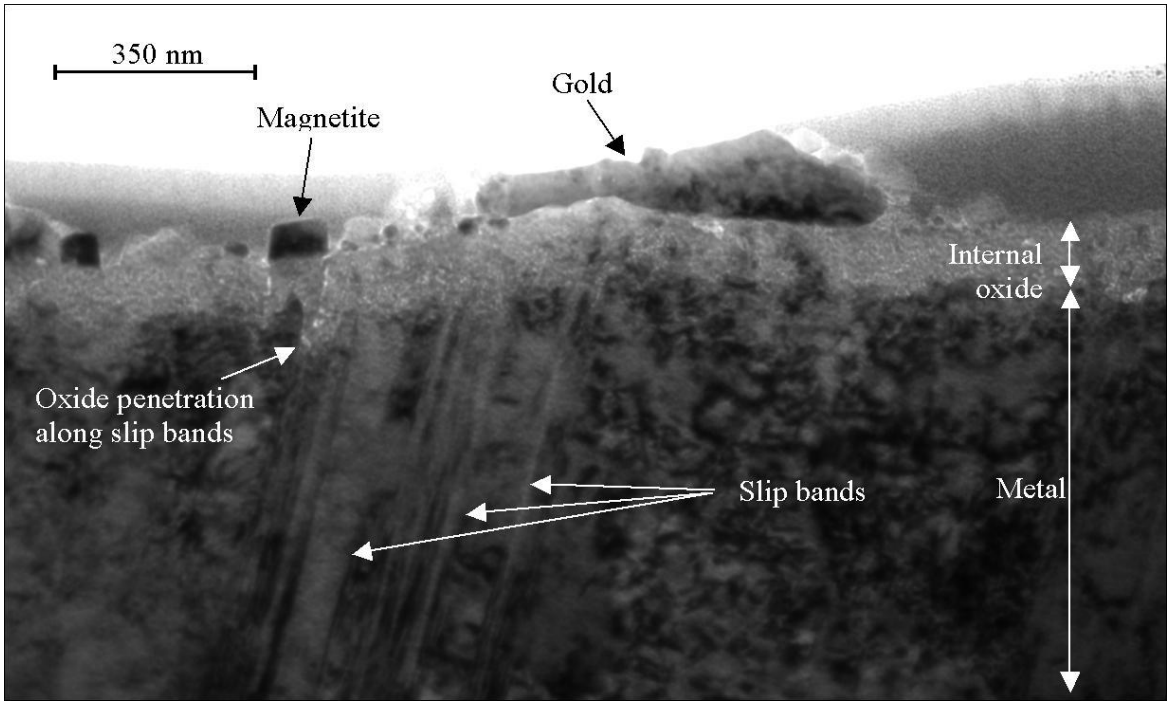

Figure 6 – Oxide observation (TEM, bright field) at site 1A on the surface of specimen 1594-T112-06 (304L).

Figure 7 is an EDS scan corresponding to the previous site (at the location of the remaining gold grid). Oxygen content is plotted in arbitrary units, while Fe, Cr, Ni and Au+Pt contents are plotted in weight %. O and Ni contents slightly increase within the 200 nm – 130 nm depth range. Conversely, Fe content decreases and Cr content does not change. It can be noticed also that Ni maximum correspond to minima in Fe and O content. This observation suggests that only a limited fraction of Ni (noble element) is affected by oxidation, contrary to Fe and Cr.

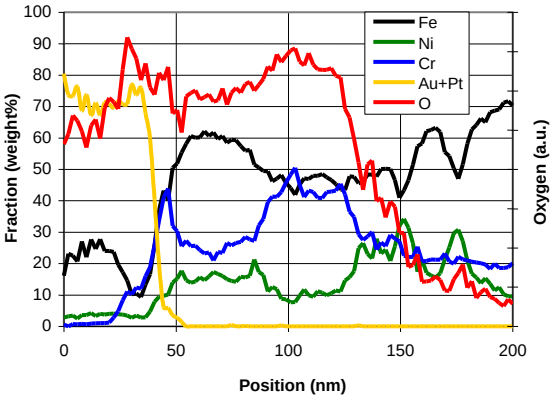

Figure 7 – EDS profile. Site 1A at the surface of specimen 1594-T112-06 (304L).

The important decrease of the Fe content indicates that oxidation essentially affects Fe. Within the range 130 nm – 90 nm, Fe and Cr contents are equivalent (45%) and significantly higher compared to Ni content (10%). Therefore, a significant Cr enrichment is observed in this inner oxide layer. It can be assumed that Fe diffusion is more effective than Cr diffusion in this layer. Within the range 90 nm – 45 nm, the oxide is essentially composed of Fe (60%), even if Cr (25%) and Ni (15%) are present. This outer oxide layer is probably essentially composed of Fe spinels. The total thickness of the oxide is approximately 150 nm, including 40 nm of Cr-rich oxide.

EFTEM maps of O, Fe and Cr are presented on Figure 8. These maps were collected at a site where no prior strain was measured, but where a significant strain (0.075) was expected during exposure to primary water. The oxygen map indicates the position of the superficial oxide and magnetite. The iron map shows the presence of an outer thin (a few nm) Fe-rich oxide layer. The chromium map reveals possible variations of Cr concentration in the inner oxide layer. The interface between the inner oxide and the metal is irregular. The areas highlighted by red rectangles on Figure 8 suggest an anisotropic oxidation at the metal-oxide interface.

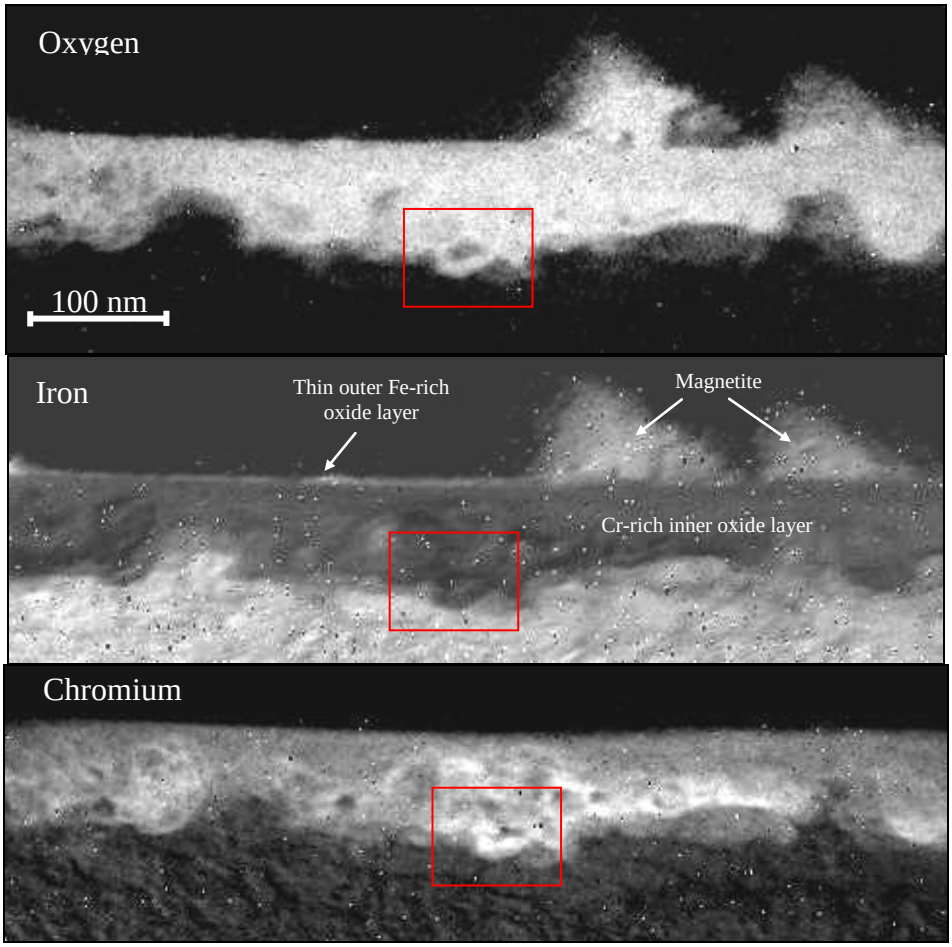

Figure 8 – EFTEM maps on site 2 at the surface of specimen 1594-T112-06 (304L). Focus (red rectangle) on anisotropic oxidation on the internal oxidation front.

Figure 9 displays a STEM observation showing possible differences in density between the outer and the inner part of the Cr-rich oxide layer. The outer part, at the interface with the spinels appears regular and dense, whereas the inner part seems to be composed of small "grains" growing inhomogeneously in the metal. The typical size of "grains" observed in the inner oxide may be compared with the characteristic length of fine dislocation structures in the underlying metal. Additionally, Figure 11 shows a significant porosity in the oxide layer at the intersection with slip bands, indicating an effect of the deformation occurring after oxidation on the metal/oxide interface and raising questions about the effects of plastic deformation on further oxidation and SCC processes.

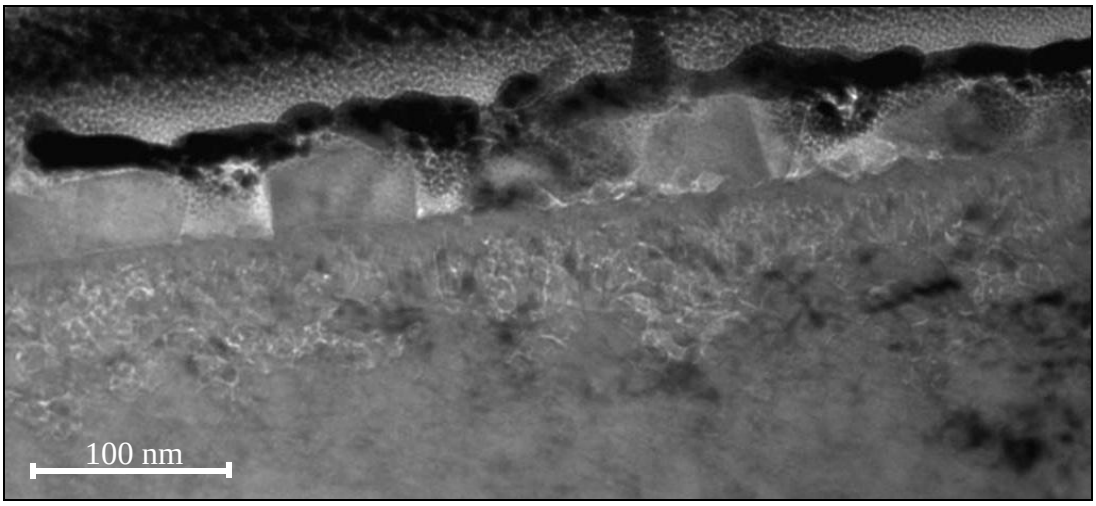

Figure 9 – TEM on site 1B at the surface of specimen 1594-T112-06 (304L).

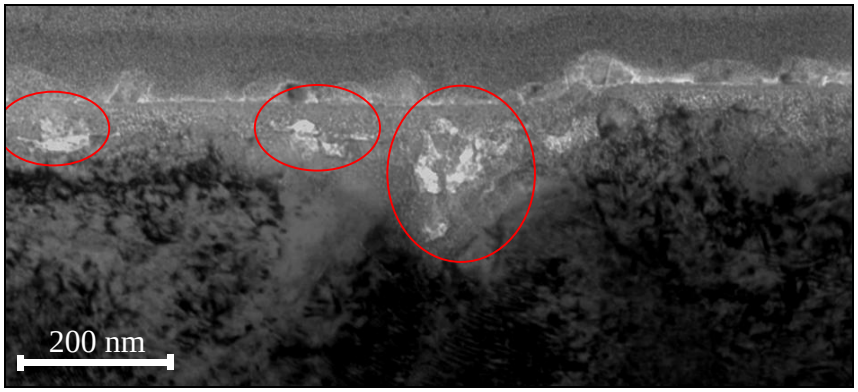

Figure 10 – Porosity in inner oxide layer, at the interface with the metal. TEM on site 2 at the surface of specimen 1594-T112-06 (304L).

Detailed analyses were carried out in order to evaluate the effect of strain localization on oxide penetration and on metal-oxide interface. **Figure** 11 shows an example of EFTEM Cr-map, with the associated binary map obtained after filtering. Image analysis of this binary map allowed to quantify the thickness of the inner Cr-rich oxide layer and perform a statistical analysis over the analyzed area (**Figure** 12). The three samples from specimen T217-01 (316L) were focused on IG crack initiation sites. This allowed the characterization of the oxide layer on both sides of the grain boundary, both grains having experienced distinct deformation levels. **Figure** 13 shows the crack initiation and Cr-layer analysis carried out on both grain around the cracked boundary on site 1 of specimen T217-01. The results obtained by image analyses of inner oxide layers are summarized in Table 5.

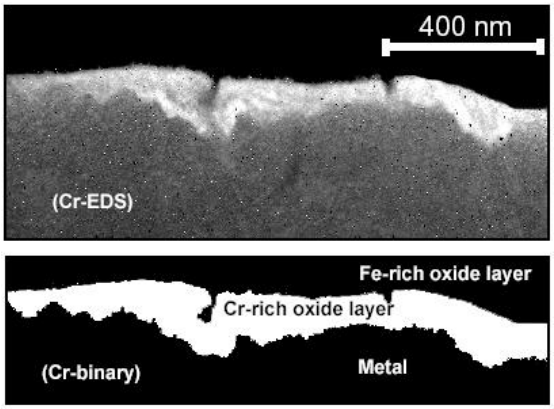

Figure 11 – EFTEM and analysis image of Cr-rich inner oxide layer at the surface of specimen T112-06 on site 1A (304L)

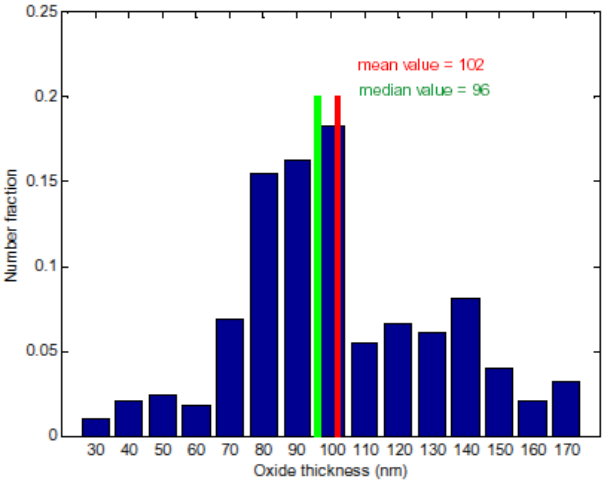

Figure 12 - Distribution of the thickness of the rich-Cr inner oxide layer formed at the surface of specimen T112-06 on site 1A (304L)

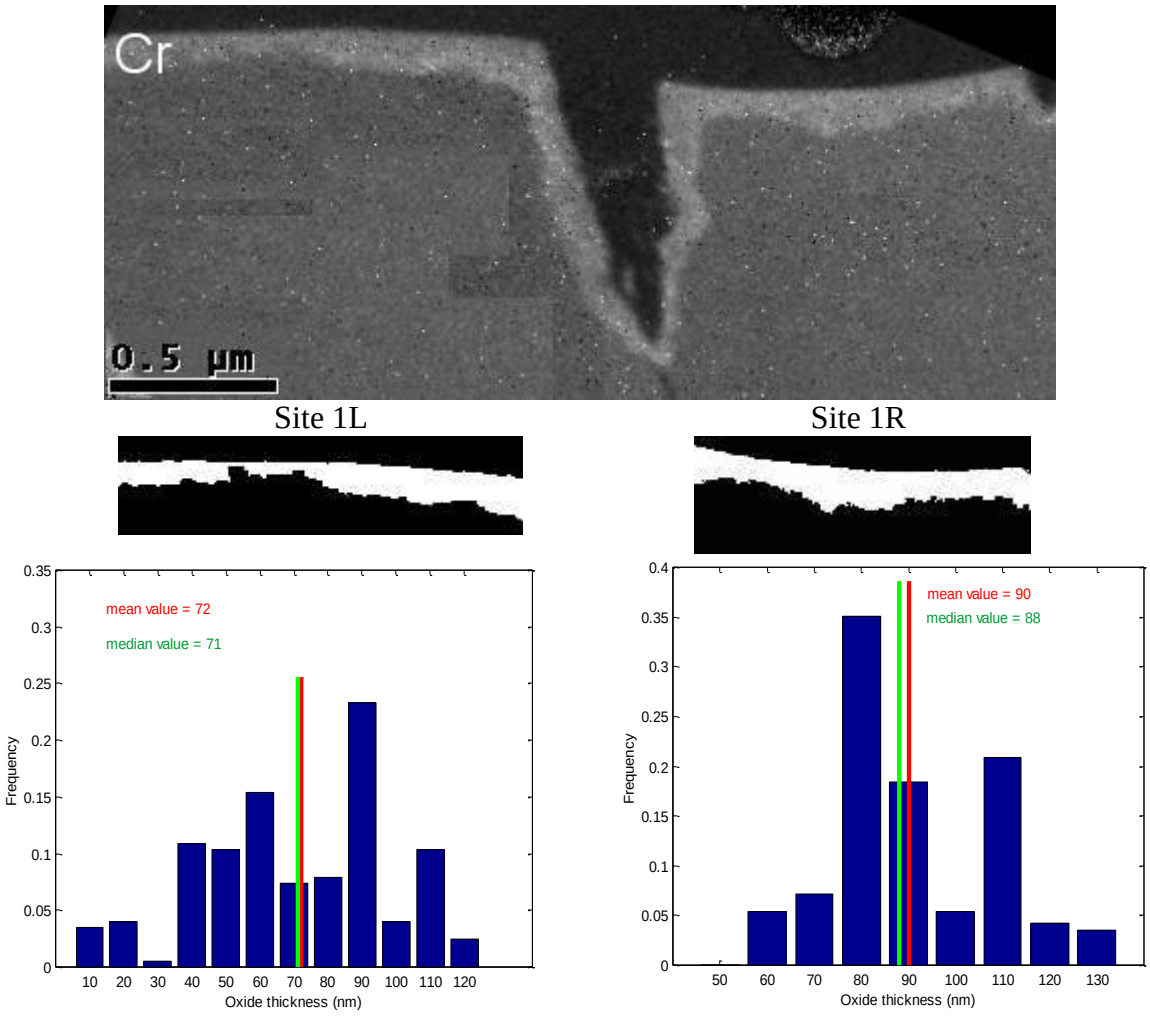

Figure 13 – EFTEM analysis of Cr-rich inner oxide layer at the surface of specimen T217-01 on site 1 (316L)

Table 5 – Analysis of Cr-rich inner oxide penetrations at the surface of cross-shaped specimens.

Specimen	Material	Site	Local strain in the sample		Cumulated strain level	Analysed length (nm)	Cr-rich inner oxide penetration (nm)				
			Prior E_{xx}	Second E_{yy}			Mean	Median	Min.	Max.	SD
T112-06	304L	1A	0.10	0.02	0,12	1386	102	96	31	172	30
		1B	0.00	0.075	0,075	694	49	49	23	87	12
		2	0.02	0.07	0,09	679	81	82	54	101	9
T217-01	316L	1L	0,05	0,05	0,10	1188	72	71	12	124	27
		1R	0,08	0,1	0,18	988	90	88	59	135	17
		2L	0	0,02	0,02	2077	46	48	6	101	25
		2R	0	0,02	0,02	890	73	74	40	105	14
		3L	0,1	0,01	0,11	2941	96	94	41	141	16
		3R	0,1	0,01	0,11	880	61	61	19	92	16

4.2. Oxides formed on material with machined surfaces

Specimen 1171-13 was a tensile specimen (grinding finish) strained to 40% deformation at room temperature and tested in the capsule during 4h at 320h. **Figure** 14 shows the analysis on site 1. The Cr-rich layer appeared fairly regular and thin (around 20 nm), only showing a significant penetration in one zone. **Figure** 16 shows the analysis of site 2, adjacent to site 1. A thin and regular layer can be observed on the right hand side, but on the left, the thickness and morphology are different: the oxide layer penetrates deeper (around 80 nm), as seen on the O map, and seems more irregular, as seen on the Cr map. The two zones probably belonged to different grains, the left one having undergone a higher level of deformation. This illustrates the complexity of real surface conditions, particularly when a significant deformation is added. Secondly, oxide penetration in the "constant thickness" zone is lower than in the cross-shaped specimen (520h and 720h exposition), indicating that oxidation processes are still active after 4h. However, maximum penetration levels are comparable. This could be an effect of the surface finish and deformation level, but would also indicate that local maxima of penetration are reached earlier and that defects possibly acting as diffusion shortcuts also enhance the oxidation kinetics.

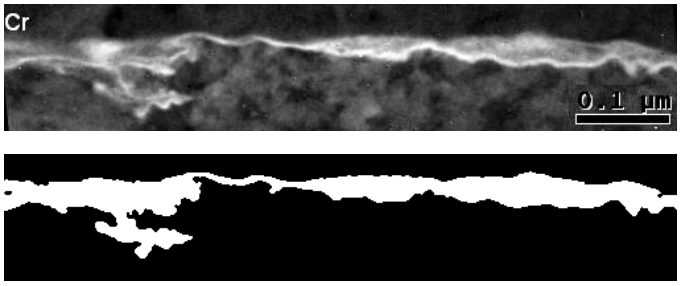

Figure 14 – EFTEM and analysis image of Cr-rich inner oxide layer at the surface of specimen 1171-13 on site 1

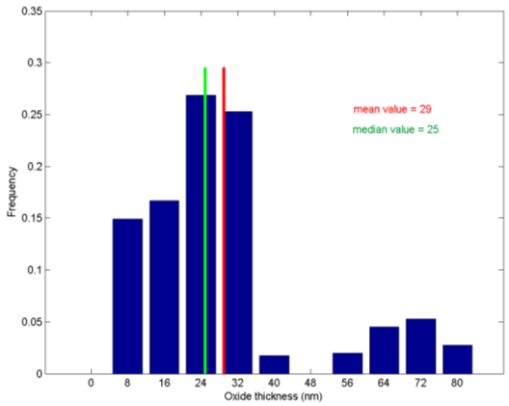

Figure 15 – Distribution of the thickness of the rich-Cr inner oxide layer formed at the surface of specimen 1171-13 on site 1

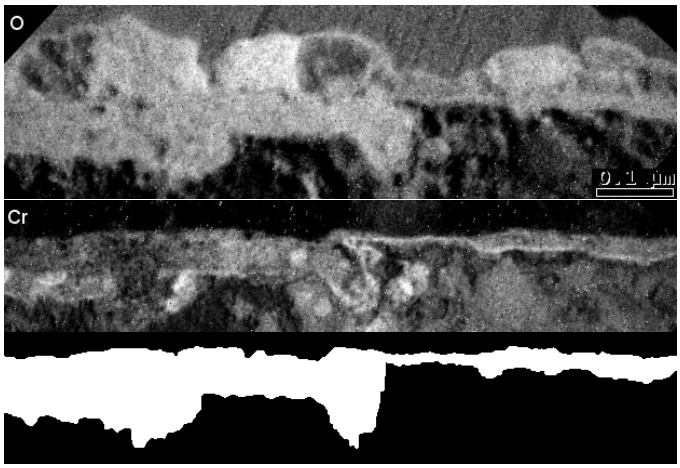

Figure 16 – EFTEM and analysis image of Cr-rich inner oxide layer at the surface of specimen 1171-13 on site 3

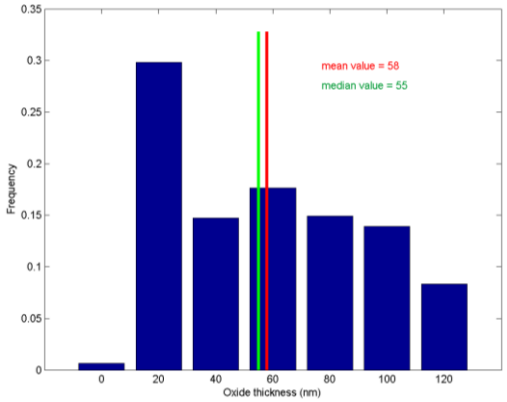

Figure 17 – Distribution of the thickness of the rich-Cr inner oxide layer formed at the surface of specimen 1171-13 on site 3

Specimens T112-35, 1171H4, 1512-10 and 1512-22 were tested in PWR water at different pH values and during various exposition times. All specimen had a grinding surface finish and samples were cut in areas unaffected by deformation in ambient air or during the test. **Figure** 18, **Figure** 19 and **Figure** 20 show Cr-rich analysis examples for specimen T112-35, 1171H4, 1512-10, exposed to environments where pH = 7.2, 8 and 9.2, respectively. They display comparable oxides morphologies with clear maxima. The oxide penetration is significantly lower at pH 7.2 and 8 (30 +/- 20 nm) than at pH 9.1 (150 +/-65 nm). On **Figure** 21 are shown the results for specimen 1512-22, also tested at pH 9.1 during 5000h (to be compared to 240h for specimen 1512-10). The penetration is more important (550 +/-70 nm) and the morphology is different: the oxide layer seems now homogeneous. Table 6 summarizes the analyses performed on specimens with machined surfaces.

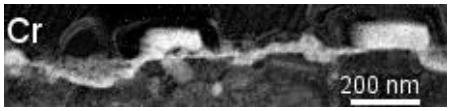

Figure 18 – EFTEM map of Cr-rich inner oxide layer at the surface of specimen T112-35 on site 2 (pH 7.2 – 17000h)

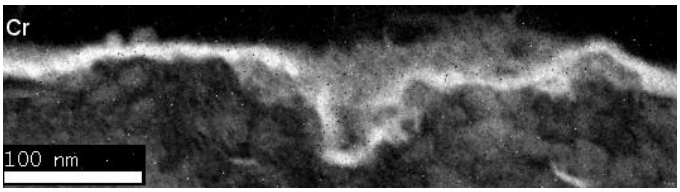

Figure 19 – EFTEM map of Cr-rich inner oxide layer at the surface of specimen 1171H4 (pH 8 – 600h)

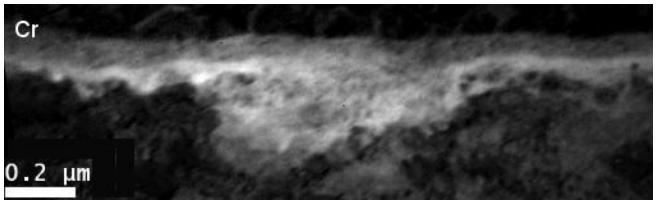

Figure 20 – EFTEM map of Cr-rich inner oxide layer at the surface of specimen 1512-10 on site 1 (pH 9.1 – 240h)

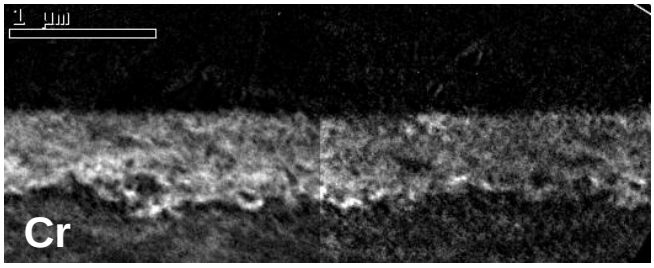

Figure 21 – EFTEM and analysis image of Cr-rich inner oxide layer at the surface of specimen 1512-22 (pH 9.1 – 5000h)

Table 6 – Analysis of Cr-rich inner oxide penetrations at the surface of the specimens without surface preparation

Material	Specimen	Site	Estimated strain	Test duration	Temperature (°C)	$pH_{320°C}$	Analysed length (nm)	Cr-rich inner oxide penetration (nm)				
								Mean	Median	Min.	Max.	SD
304L	1171-13	site 1	0,4	4	325	7.2	718	**29**	25	4	82	19
		site 2					455	**22**	24	3	38	9
		site 3					879	**58**	55	10	131	35
304L	T112-35	site 1	0.025	17000	360	7.2	1787	**59**	53	13	140	30
		site 2					1243	**35**	27	11	81	20
316L	1171H4	-	0.025	600	360	8	534	**33**	22	9	95	23
316L	1512-10	site 1	0.025	240	360	9.1	1303	**151**	121	79	279	63
		site 2	0.025				465	**139**	114	80	246	57
304L	1512-22	-	0.025	5000	360	9.1	4383	**552**	542	383	725	66

4.3. Observations on intergranular crack initiation sites

Each of the three samples from specimen T217-01 was located on an intergranular crack initiation site. It was thus possible to conduct the analysis along the crack together with the adjacent free surfaces. Observed intergranular crack tips were most likely active, as the cracks only affected on boundary (no branching). Cracks usually initiated where discontinuities of deformation across grain boundaries were the most prevalent, as illustrated with local deformation measurements in **Figure** 4 and **Figure** 5. STEM images of the cracks, seen in **Figure** 22, **Figure** 23, **Figure** 24 and **Figure** 25, clearly exhibit cracks along grain boundaries separating grains with different densities of dislocations.

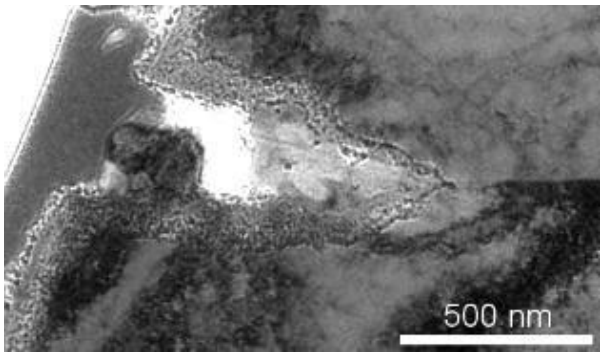

Figure 22 – Bright field image of the crack initiated at site 1 of specimen T217-01

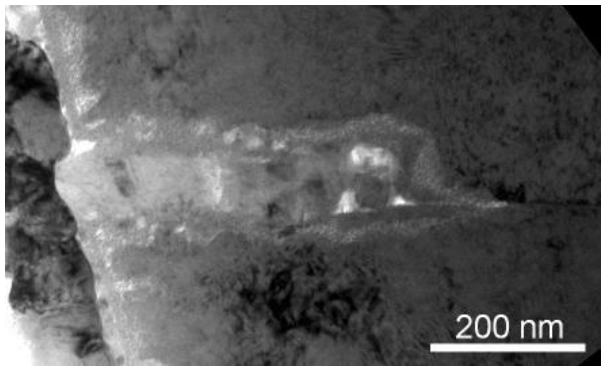

Figure 23 – Bright field image of the crack initiated at site 2 of specimen T217-01

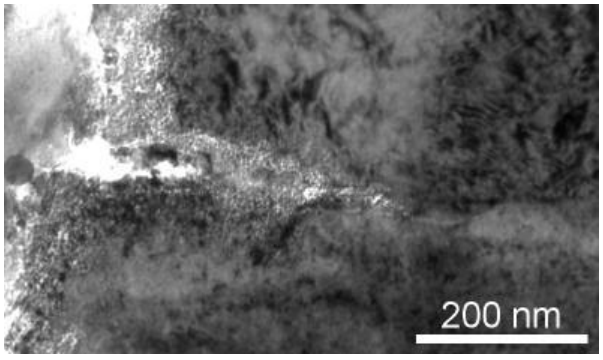

Figure 24 – Bright field image of the crack initiated at site 3 of specimen T217-01

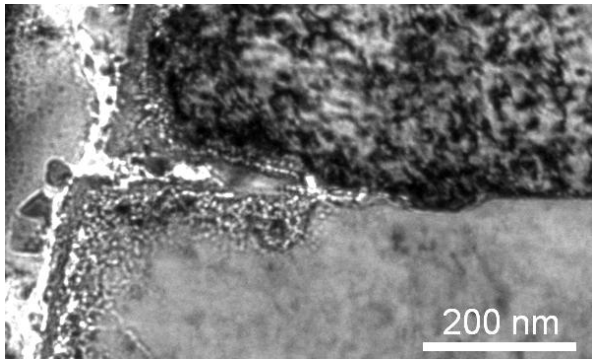

Figure 25 – Different dislocation densities between grains. Defocused bright field image of the crack initiated at site 3 of specimen T217-01

Crack depths did not exceed a few microns and the typical crack mouth opening displacement was about 200 nm. Open cracks were filled with Fe oxide (Figure 27). Crack walls exhibited a

regular Cr-rich oxide layer whose morphology and thickness were comparable to that of the surrounding free surfaces. This would indicate that the local environmental conditions were essentially unaffected by the presence of iron oxide and that the time to stabilize the Cr oxide layer was probably significantly shorter than the testing time. The opening of the cracks was dissymmetric with respect to the grain boundary. This may be due to stress relaxation along the grain boundary after cracking, with plastic deformation in the "softer" grain possibly enhancing further dissolution in this grain by a local destabilization of the passive film.

At the crack tip, oxide penetration was deeper along the grain boundary than below the free surfaces. This may be due to the grain boundary acting as a short-circuit for oxygen diffusion. In addition, the non-oxidized grain boundaries ahead of the crack tip showed significant compositional changes over more than 100 nm ahead of the intergranular oxide. This can be compared to what was seen at the metal-oxide interface over only a few nm: a significant enrichment in nickel, with associated depletion in iron and chromium. This phenomenon may also be related to the free volume of the grain boundary, allowing the oxidation phenomenon to operate deeper and promoting a faster diffusion of Cr and Fe. The implications on the oxidation mechanisms, the mechanical behavior of the boundary and the cracking could be considerable. Table 7 summarizes the analysis performed for each crack, taking into account the crack length, the oxidation of the crack tip, the affected zone ahead of the tip and the structure of the crack walls.

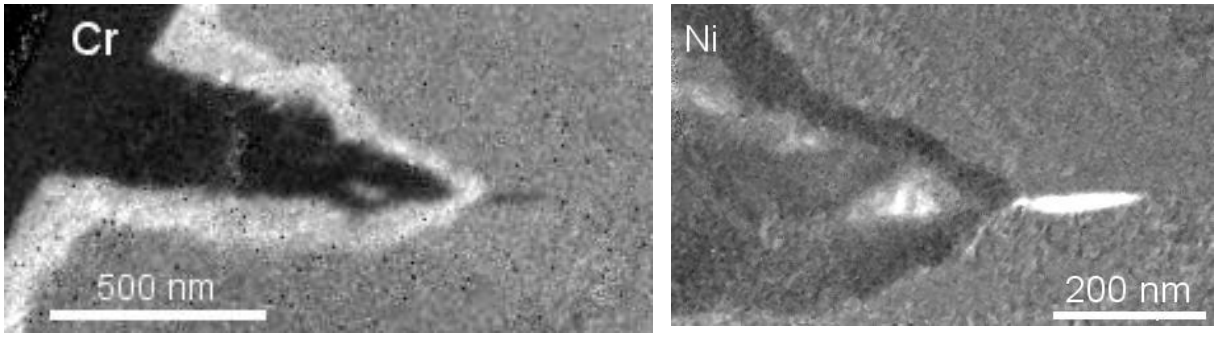

Figure 26 – EFTEM analysis of Cr-rich inner oxide layer and Ni enrichment in grain boundary ahead of the tip in the crack initiated at site 1 of specimen T217-01

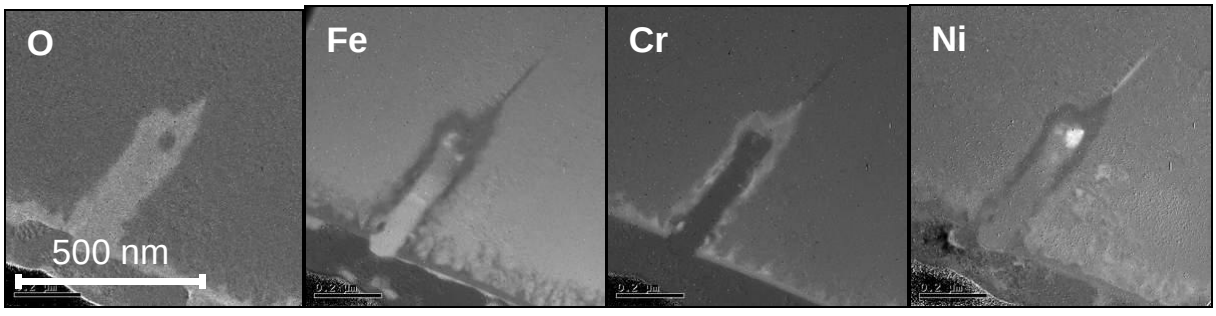

Figure 27. O, Fe, Cr and Ni EFTEM maps of the crack initiated at site 2 on T217-01

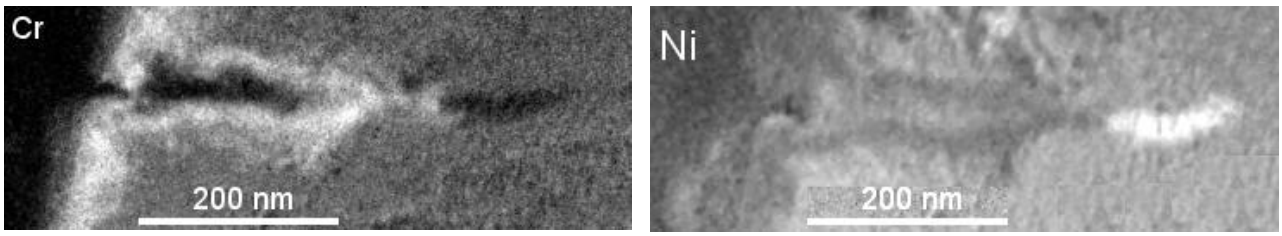

Figure 28 – EFTEM analysis of Cr-rich inner oxide layer and Ni enrichment in grain boundary ahead of the tip in the crack initiated at site 3 of specimen T217-01

Table 7 – Analysis of the cracks initiated at the surface of of specimen T217-01 (316L - 720h - pH 7.2)

Crack	Site	Local strain in the sample		Crack length (nm)	Oxide at the crack tip (nm)	Affected grain boundary length (nm)	Analysed length (nm)	Cr-rich inner oxide penetration (nm)				
		Prior E_{xx}	Second E_{yy}					Mean	Median	Min.	Max.	SD
1	left	0,05	0,05	899	59	170	786	**88**	89	48	119	16
	right	0,08	0,1				619	**76**	83	24	125	28
2	left	0	0,02	548	136	136	304	**67**	66	50	89	9
	right	0	0,02				322	**66**	64	56	82	7
3	left	0,1	0,01	317	110	125	123	**43**	43	33	52	5
	right	0,1	0,01				143	**36**	38	16	47	7

5. Discussion

5.1. Effect of deformation

Figure 29 shows the evolution of chromium-rich oxide penetrations as a function of cumulated deformation. The mean oxide penetration increases for higher deformation levels as well as the extrema. A sharp increase appears around 10 % cumulated deformation. This phenomenon could be explained by the features observed in Figure 6 and Figure 9. Oxidation phenomena seem to interact with plastic deformation by different mechanisms. The preferential oxidation along the deformation structures could explain this behavior, from the dislocation network increasing the mean penetration (Figure 6) to slip bands setting local maxima of penetration. Defects may act as diffusion sort-circuits for oxidizing species and allow the oxidation to penetrate deeper within the metal surface.

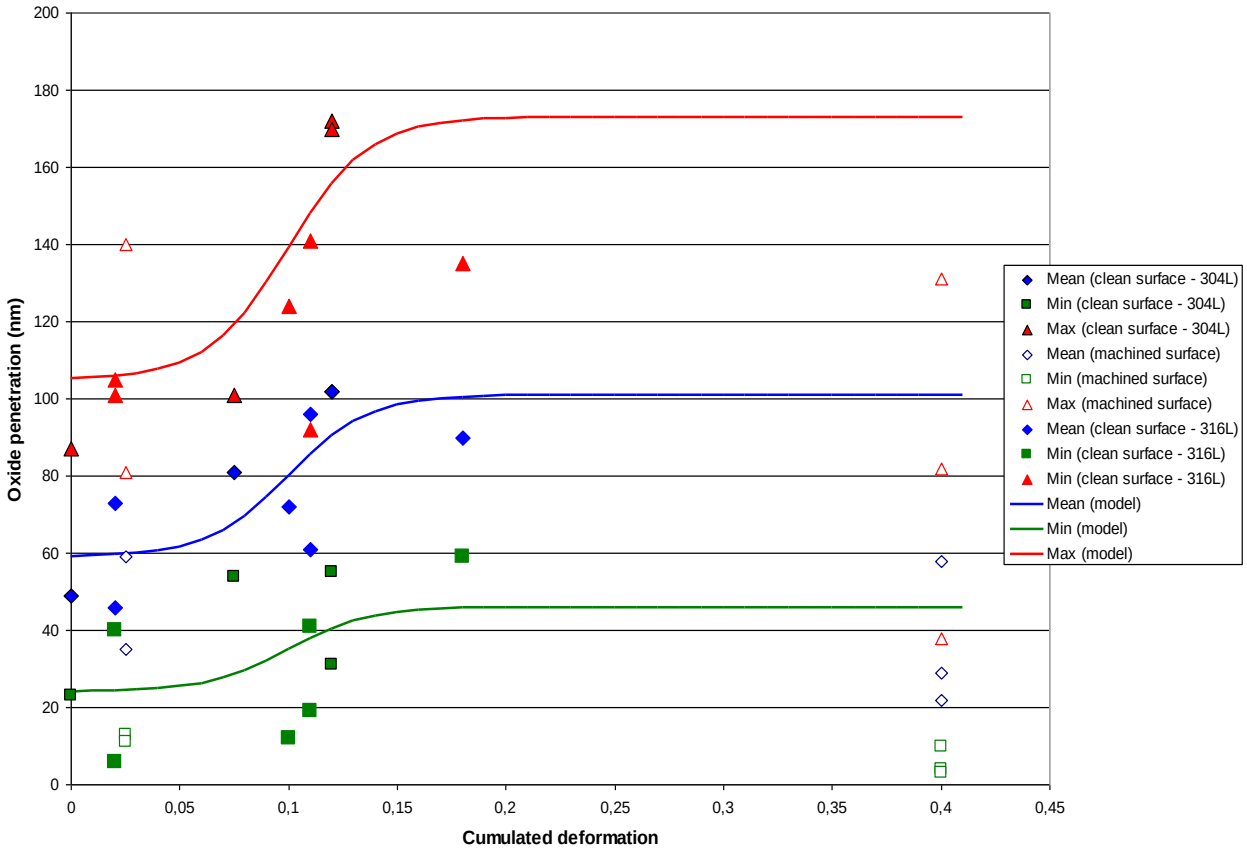

Figure 29 – Evolution of the Cr-rich oxide penetration as a function of cumulated deformation

5.2. Effect of the pH of the environment

Figure 30 shows the effects of pH on the oxide growth, using the results from tests on specimen with machined surfaces. First, a decrease on the oxide penetration can be seen at pH 8 and a significant increase at pH 9.1. Secondly, comparing the durations of the various tests at pH 7.2 and pH 9.1, pH could also have a significant impact on the oxide penetration kinetics. At pH 7.2, stabilization of the Chromium passive layer seems to occur after a few hours of exposition ; 40 nm after 4h, 50 nm after 17000h (50 nm after 500h for cross test specimen on low deformation areas). On the other hand, at pH 9.2 the oxide is still actively penetrating the metal surface after hundreds of hours (150 nm after 240h, 550 after 5000h). **Figure** 31 illustrates the possible evolution of the average oxide penetration as a function of time for pH 7.2 and pH 9.1, fitting the result and assuming a saturating law (Evans type). This would indicate a critical change in chemical behavior, bringing into question the passivity of the chromium layer at pH 9.2, as well as pointing out possible effects of occluded environments of high alkalinity on oxide growth and SCC cracking.

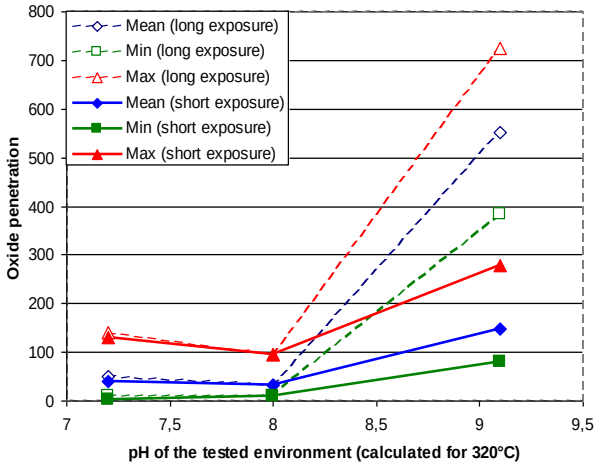

Figure 30 – Oxide penetration as a function of pH (machined surfaces)

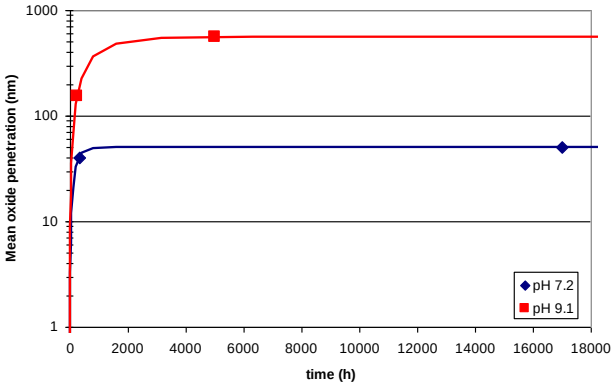

Figure 31 – Mean oxide penetration as a function of time for pH 7.2 and pH 9.1, fitting results from the test with saturating laws (Evans-type)

5.3. Cracks analysis

The crack tip in site 1 exhibits a different morphology; closer to the tip, the oxide layer on the crack walls gets thinner and the crack tip doesn't show any preferential oxidation along the grain boundary. The crack is twice longer (almost 1 µm) than the other so this could be seen as an effect of the crack length: the transport of the oxidizing species is less effective the longer the crack is. Additionally, the grain boundary ahead is also the most affected (almost 200 nm): the tip and affected region sum up to reach an equivalent level the other cracks. This fact could mean that the crack was still active at the end of the test, the oxidation processes not yet stabilized, and would indicate that the cationic diffusion of the metallic species (chromium and iron) is precursory to the oxidation (anionic diffusion of oxygen).

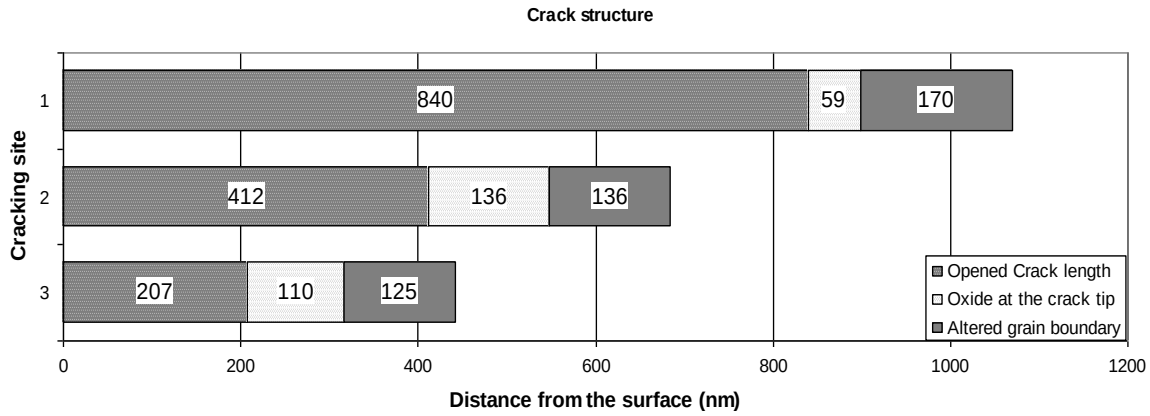

Figure 32 – Comparison of crack structures

Figure 33 shows the evolution of oxidation depth along the crack walls and crack length as a function of local deformation during the test (second E_{yy}). Observations are consistent with the surface observations, indicating a deeper penetration in areas with higher levels of deformation. Crack length seems to be correlated to local deformation in a similar way. Again, the crack at site 1 stands out, as seen on the EFTEM image (**Figure** 26). At a higher level of deformation, it is the longest crack and highest maximum oxide penetration along the crack walls. However, as indicated above, closer to the tip, the oxide thickness decreases. This may indicate that the crack was still active at the end of the test, achieving a deeper penetration and passivity where the crack initiated and thinner penetration in later exposed surfaces after a propagation step. From this case, and assuming the other two cracks experienced only one cracking event, this would indicate that the typical intergranular cracking step is between 200 nm and 500 nm. This information is valuable for the general understanding of SCC mechanisms, as it defines an area where investigations about the cracking factors should be led, and sets a representative length scale for future mechanistic modeling of intergranular cracking.

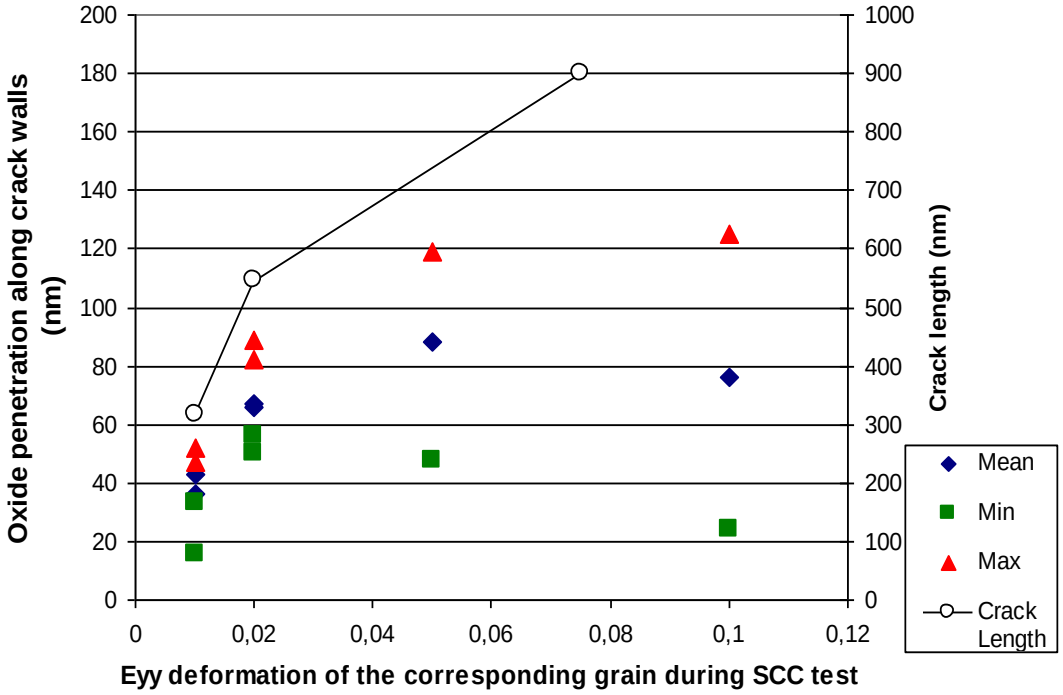

Figure 33 – Oxidation of the crack walls and crack length as a function of deformation

5.4. Assessed cracking mechanism

Based on previous considerations, the following basic mechanism is assumed to explain both initiation and propagation of SCC in stainless steels exposed to primary water :

1. Oxidation, leading to the formation of a superficial Cr-rich passive layer with a mean thickness of 50 nm. The maximum oxide penetration does not exceed 90 nm at 360°C, when 7 < pH320°C < 8, if the material is not strain hardened.

2. When sufficient, local stresses lead to the fracture of the oxide or metal-oxide interface. Strain hardening, loading fluctuations, intergranular strain incompatibilities and irregular metal-oxide interfaces promote stress concentrations and, as a consequence, initiation or crack tip extension.

Judging from observations, transgranular cracks are supposed to initiate on intense slip bands preferentially oxidized and strained during exposure while intergranular cracks initiate after preferential oxidation along grain boundaries and stress concentrations appearing between grains.

6. Conclusion

Oxidation of free surfaces and IGSCC cracks of cold-worked austenitic stainless steels exposed and strained in PWR water have been characterized by ATEM of cross-sections samples. Oxidation at free surfaces consists in an outer Fe-rich oxide layer and an inner Cr-rich oxide, and appears clearly below the original surface of the material. The oxide layer seem to penetrate deeper along deformation features and microstructural defects such as the dislocation network, slip band or grain boundaries. The assumed growth mechanism is by anionic processes, diffusion of oxygen allowing penetration of the oxide and defects acting as diffusion short-circuits. The sparse magnetite spinels found at the surface of the oxide layer most likely grow by a cationic mechanism. Judging from local deformation measurements, oxide penetration seem to increase with deformation of the material with a strong increase around 10 % local deformation. Alkalinity seems to affect oxide penetration: compared to the nominal pH 7.2 water, pH 8 shows a reduced penetration while pH 9.1 exhibits a significant penetration as well as altered kinetics.

Intergranular crack initiation was also characterized by ATEM. Initiation occurred at boundaries separating grain with seemingly different levels of plastic deformation. Cracks were filled with Fe-rich oxide and crack-wall exhibited a Cr-rich oxide penetration similar to that of the free surfaces. Grain boundaries at the crack tip exhibited preferential oxide penetration and a zone ahead of the oxidized tip revealed significant depletion in both Fe and Cr, with an according enrichment in Ni.

Results on machined surfaces emphasized the complexity of the phenomenon in real conditions. An upcoming study of surface finish effects is being performed on a set of samples oxidized in the same conditions (nominal PWR, 150h), with different surface preparation.

Short time exposure in the capsule and crack initiation analysis also revealed that the stability of the Cr-rich passive layer is reached after a few hours and set a higher bound for the investigation of oxidation kinetics. In this perspective, a device allowing short-time exposures (from a minute to tens of hours) is currently under development.

References

1. T. Couvant, F. Vaillant, JM. Boursier, D. Delafosse, 'Effect of strain path on SCC of AISI 304L stainless steel in PWR primary environment at 360°C', (Paper presented at Eurocorr'2004, Nice, France, 2004).
2. T. Couvant, L. Legras, C. Pokor, F. Vaillant, Y. brechet, J.M. Boursier, P. Moulart, 'Investigations on the mechanisms of PWSCC of strain hardened austenitic stainless steels', 13th International Conference on environmental degradation of materials in nuclear systems-water reactors, Whistler (Canada), 2007.
3. Angel, 'Formation of martensite in austenitic stainless steels', *Journal of the Iron and Steel Institute*, 177 no 1 (1954), 165-174.
4. Lacombe, Béranger, 'Structures et diagrammes d'équilibre des diverses nuances d'acier inoxydables. Conséquences sur leurs traitements thermiques', Les aciers inoxydables, éd. P. Lacombe, pp. 13-58, 1990.
5. T. Couvant, L. Legras, A. Herbelin, A. Musienko, Q. Vertenelle, G. Ilevbare, D. Delafosse, G. Cailletaud, J. Hickling, " Development of understanding of the interaction between localized deformation and SCC of austenitic stainless steels exposed to primary PWR environment", Eurocorr 2008.
6. T. Couvant, L. Legras, A. Herbelin, A. Musienko, G. Ilevbare, D. Delafosse, G. Cailletaud, J. Hickling, " Development of understanding of the interaction between localized deformation and SCC of austenitic stainless steels exposed to primary PWR environment", 14th Conference on Environmental degradations of materials in nuclear systems-water reactors, Virginia Beach (USA) 2009.